Interlayer coupling and magnetoresistance of MnGa-based trilayers with semiconducting, antiferromagnetic, and ferrimagnetic spacer layers

W. Van Roy*
Joint Research Center for Atom Technology–Angstrom Technology Partnership (JRCAT-ATP), 1-1-4 Higashi, Tsukuba, Ibaraki 305-0046, Japan

H. Akinaga†
Joint Research Center for Atom Technology–National Institute for Advanced Interdisciplinary Research (JRCAT-NAIR), 1-1-4 Higashi, Tsukuba, Ibaraki 305-8562, Japan

S. Miyanishi‡
Joint Research Center for Atom Technology–National Institute for Advanced Interdisciplinary Research (JRCAT-NAIR), 1-1-4 Higashi, Tsukuba, Ibaraki 305-8562, Japan
and Institute of Materials Science, University of Tsukuba, 1-1-1 Tennoudai, Tsukuba, Ibaraki 305-0006, Japan
(Received 4 October 2000; published 18 April 2001)

We have studied the influence of the magnetic structure of the spacer layer on the interlayer exchange coupling and on the correlation between the coupling and magnetoresistance in MnGa-based trilayers with antiferromagnetic (Mn_2As), ferrimagnetic (Mn_2Sb), and semiconducting (GaAs) spacer layers. The samples are grown epitaxially on GaAs(001) substrates using molecular beam epitaxy. We can control both the period of the magnetic long-range order in the spacer layers and the orientation of their easy axis with respect to the MnGa easy axis. Magnetic measurements show that the *period* of the interlayer coupling is *not related* to the magnetic long-range order of the spacer layer. The *strength* of the coupling *does depend* on the orientation of the easy axis of the spacer, with strong coupling when it is collinear with the easy axis of MnGa and weak coupling when it is orthogonal. GaAs spacer layers grown using an optimized procedure to eliminate any Mn contamination still show metalliclike behavior. This is attributed to a large defect density caused by the low-temperature growth. The sign and magnitude of the magnetoresistance show a direct correlation with the interlayer coupling. The proportionality constant is universal for all spacer layer materials under investigation. This behavior is discussed in terms of two models based on quantum interference effects and on a frustration magnetoresistance mechanism.

DOI: 10.1103/PhysRevB.63.184417 PACS number(s): 75.70.Cn, 75.70.Pa, 81.15.Hi

I. INTRODUCTION

A. Motivation

Interlayer exchange coupling (IEC) and giant magnetoresistance (GMR) in magnetic multilayers have been studied intensively during the last decade.[1] Most of the work has been done on metallic, nonmagnetic spacer layers. In the case of semiconducting spacer layers, the coupling strength was very weak (0.005 mJ/m^2 for amorphous Si spacer layers in Fe/*a*-Si/Fe trilayers grown at 77 K,[2] compared to values up to 5 mJ/m^2 for metallic spacers[3]), but it could be thermally induced.[2,4–6] Many of the subsequent experiments at room temperature suffered from the formation of various iron silicides due to the reactivity between iron and silicon, resulting in a poor understanding of the electronic properties of the spacer layers. Chaiken *et al.*[7] suggested that the spacer layers in antiferromagnetically coupled Fe/Si multilayers were crystalline and metallic, and that the coupling has the same origin as in metal/metal multilayers. Recently, Endo *et al.*[8,9] showed the telltale positive temperature coefficient of coupling through a nonmetallic spacer and used a mixture of metallic and insulating phases to fit their results.

Motivated by the work on epitaxial TM-III/III-V heterostructures (TM=transition metal) such as NiGa/GaAs and CoGa/GaAs,[10] we have studied GaAs spacer layers in (nominally) MnGa/GaAs/MnGa trilayers and found a strong interlayer coupling up to 0.35 mJ/m^2 at room temperature.[11] Even more surprising was the clear correlation between the signs of the magnetoresistance and interlayer coupling. Samples with ferromagnetic (F) and antiferromagnetic (AF) interlayer coupling showed normal and inverse ''GMR,'' respectively.[12] However, understanding of these phenomena was hampered by a magnetic contamination of the spacer layers as the result of Mn diffusion at the elevated growth temperature (300 °C), with Mn concentrations up to 50 at. % and resulting in the formation of a mixed phase between GaAs and Mn_2As with uncontrolled electronic and magnetic properties.

One obvious way to gain a better understanding is to reduce the Mn contamination. The growth and structural properties of GaAs spacer layers without detectable Mn contamination were reported earlier.[13] The magnetic properties of the trilayers with improved GaAs spacers will be presented here.

The second approach, and the main subject of this paper, is to directly study the influence of the magnetic structure of the spacer layers. Indeed, the extensive treatment of the interlayer exchange coupling in terms of quantum interferences by Bruno[6] is valid only for nonmagnetic spacer layers. It cannot be applied when long-range magnetic order is present in the spacer layer. Although one can expect quantum-size

 ©2001 The American Physical Society

effects to persist, they would be superimposed on the effects of direct coupling between the moments in the ferromagnetic films and in the magnetic spacer, similar to the exchange biasing of a ferromagnetic film by an antiferromagnetic layer in spin valve structures.[14] The relative orientation of both ferromagnetic (FM) films (i.e., the interlayer coupling between them) would then be determined by the relative orientation of the moments in the top and bottom planes of the spacer. The spacer layer thickness dependence of the IEC would mimic the internal magnetic structure of the spacer layer and would not be related to quantum interference effects. We present here an experimental investigation of the role of the internal magnetic period of the spacer layer and the orientation of its quantization axis with respect to that of the ferromagnetic films using well-controlled antiferromagnetic Mn_2As and ferrimagnetic Mn_2Sb spacer layers.

Third, a better understanding of the IEC is also important for the interpretation of the magnetoresistive behavior of the samples. Barnas and Bruynseraede[15] have predicted a correlation between quantum-size effects in the giant magnetoresistance and interlayer coupling in magnetic multilayers which is consistent with our experimental results. However, this model cannot be applied if the coupling is from a different origin (direct coupling similar to exchange bias effects). Alternatively, we have proposed a phenomenological frustration magnetoresistance model that explains the correlation in terms of a frustration of the magnetic moments of MnGa near the interfaces with the spacer layer.[12] It makes abstraction of the specific coupling mechanism and can be applied to the case of direct coupling as well. We will present magnetoresistance data for semiconducting, antiferromagnetic, and ferrimagnetic spacer layers, and discuss their correlation with the IEC in terms of both models.

B. Material system

The δ phase of MnGa is one of several ferromagnetic phases formed by Mn and Ga.[16–19] It has a tetragonal crystal structure with CuAu type-I ordering (Fig. 1, center) and shows strong magnetocrystalline anisotropy with the c axis as easy axis and an anisotropy field $\mu_0 H_a = 2K_u/M_s \approx 6.4\,\mathrm{T}$,[18] where the saturation magnetization M_s varies from 510 to 450 kA/m over the bulk stability range of 56–59 at. % Mn.[16] The in-plane lattice parameter $a_{\mathrm{MnGa}} = 0.272\,\mathrm{nm}$ is only 4% smaller than half of the lattice parameter of GaAs ($a_{\mathrm{GaAs}}/2 = 0.283\,\mathrm{nm}$), allowing the epitaxial growth of single-crystalline films on GaAs(001) substrates using molecular beam epitaxy (MBE).[20] The c axis grows perpendicular to the GaAs(001) surface, resulting in thin films with a perpendicular magnetization. The films show square hysteresis loops, and we have demonstrated previously that it is possible to modify the coercive field by controlling the composition and the post-growth thermal treatment.[21]

The strong perpendicular anisotropy of MnGa thin films has two important advantages. It limits the possible direction of the magnetization of each FM film to two distinct states (up and down along a single axis) and results in hysteresis loops with well-defined plateaus. The absence of noncollinear states greatly facilitates the analysis of the measurements. The perpendicular magnetization also allows the use of transport measurements [the extraordinary Hall effect (EHE)] to determine the magnetic hysteresis loops and thus the IEC simultaneously with the magnetoresistance (MR).

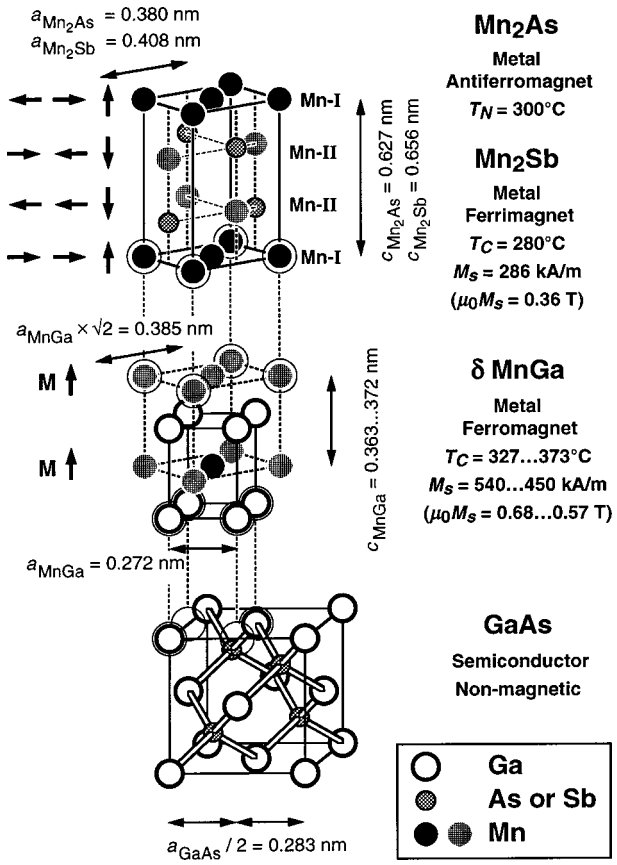

FIG. 1. Crystal structure and epitaxial relationship for the materials used in this work. Bottom: GaAs, zinc-blende unit cell. Center: MnGa, tetragonal unit cell with CuAu type-I ordering or ordered body-centered-tetragonal (bct) (solid lines). The nonstandard face-centered-tetragonal (fct) unit cell which is $\sqrt{2}$ times larger and rotated over 45° is shown as well using shaded circles and dotted lines. Top: Mn_2As and Mn_2Sb crystallize in the Cu_2Sb-type tetragonal structure with two nonequivalent Mn sites, labeled Mn-I and Mn-II. The orientation of the present trilayers is GaAs(001)[100]‖MnGa(001)[100]‖Mn_2As or Mn_2Sb(001)[110].

Mn_2As (Refs. 22–24) and Mn_2Sb (Refs. 25–30) both have the Cu_2Sb-type tetragonal crystal structure (Fig. 1, top). The basal plane lattice constants $a_{\mathrm{Mn_2As}}$ and $a_{\mathrm{Mn_2Sb}}$ are larger than a_{MnGa} by a factor very close to $\sqrt{2}$. In fact, when the unit cell is rotated by 45° around the c axis the crystal structure is identical to MnGa except for the insertion of an additional layer of atoms on the vertical faces of the cell. The lattice mismatch with the basal plane of MnGa is −1.3% and +6.0% for Mn_2As and Mn_2Sb, respectively. We have already shown the epitaxial compatibility in the growth of single-crystalline Mn_2As(001) films on MnGa and GaAs,[31] as well as Mn_2Sb(001) on GaAs.[32]

From the magnetic point of view, Mn_2As and Mn_2Sb have a layered structure with two nonequivalent Mn positions (Fig. 2). Planes of Mn-I atoms are sandwiched between composite planes consisting of Mn-II and As (or Sb) to form

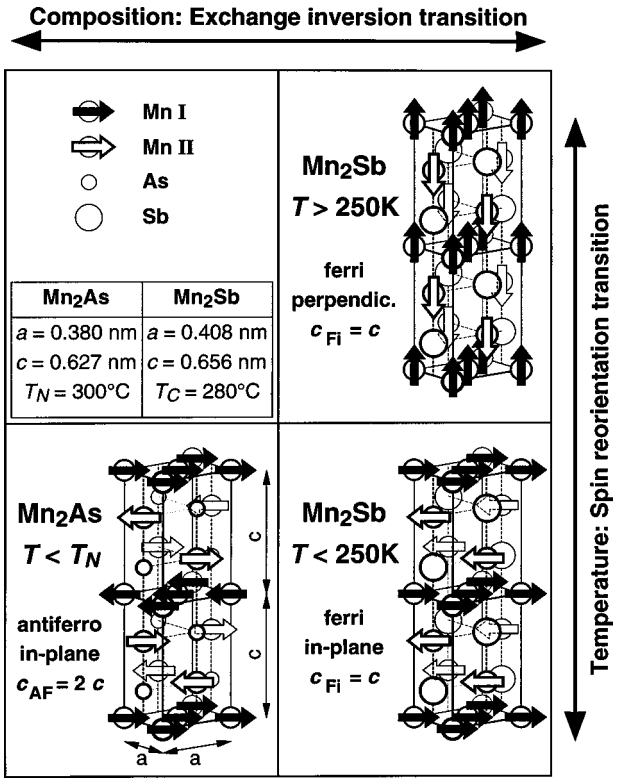

FIG. 2. Magnetic structures of bulk Mn_2As and Mn_2Sb. Here Mn_2As is a layered antiferromagnet with magnetic period equal to $2c_{Mn_2As}$. The moments are orthogonal to the c axis. Mn_2Sb is a layered ferrimagnet with magnetic period equal to c_{Mn_2Sb}. The moments undergo a spin reorientation transition from spins in the basal plane for $T<250$ K (bottom) to spins parallel to the c axis for $T>250$ K (top).

triple layers. The exchange interaction within these triple layers is strong with antiferromagnetic alignment between Mn-I and Mn-II planes.[30] Because of the different moments on Mn-I and Mn-II, the triple layers carry a net magnetic moment. The exchange interaction between the triple layers is much weaker and depends on the interatomic distance.

In Mn_2As the coupling between the triple layers is antiferromagnetic, resulting in a layered antiferromagnetic structure with magnetic period equal to 2 times the structural lattice constant $c_{AF}=2\ c_{Mn_2As}=1.254$ nm as shown in Fig. 2 (left). The moments lie in the basal plane,[23] orthogonal to the easy axis of MnGa. Here Mn_2Sb has a slightly larger lattice constant $c_{Mn_2Sb}=0.656$ nm, causing ferromagnetic alignment of the triple layers and a layered ferrimagnetic structure with magnetic period equal to the structural period $c_{Fi}=c_{Mn_2Sb}$ (Fig. 2, right). By comparing Mn_2As and Mn_2Sb spacers, we can evaluate the influence of the internal magnetic period of the spacer layer on the interlayer exchange coupling.

In addition, Mn_2Sb shows a spin reorientation transition from moments along the c axis above $T\approx250$ K to moments in the basal plane below this temperature, without affecting the antiparallel alignment of the moments. This transition has been attributed to a different temperature dependence of competing anisotropies at the Mn-I and Mn-II sites, favoring moments parallel to the c axis and in the basal plane, respectively.[25–28] The temperature dependence of IEC through Mn_2Sb spacers will clarify the role of the relative orientation of the quantization axis of the spacer layer with respect to that of the ferromagnetic films.

II. EXPERIMENT

The samples have been grown by MBE. The system consists of two growth chambers that are connected under ultrahigh vacuum. The first chamber has standard evaporation cells for Ga, As, and Si, and is used for the growth of GaAs buffer layers. The second chamber is a modified Riber 32P chamber equipped with solid-source effusion cells for Mn, Ga, and Sb, and a valved cracking cell for As.

A linear shutter in front of the substrate allowed the growth of wedge-shaped layers for a more precise study of the spacer layer thickness dependence of the magnetic properties. The wedges are typically 36 mm long with a slope of 0.5–0.7 Å/mm. The wedges were nominally stepped with a width of 2–4 mm/step. However, as a result of the large separation between the linear shutter and substrate, the steps were smoothed out and could not be resolved by the measurements. All samples were covered by a 15-nm-thick GaAs cap layer (polycrystalline or amorphous) to prevent oxidation.

Both growth chambers are equipped with a 25-keV reflection high-energy electron diffraction (RHEED) system. An Auger electron spectroscopy (AES) setup (Anelva AAS-200) is mounted on one of the transfer modules for semi *in situ* compositional analysis. X-ray diffraction (XRD) θ-2θ spectra have been taken on a Rigaku RINT-1500 diffractometer.

The magnetic properties have mainly been studied using magnetotransport measurements. Because of the perpendicular magnetization of MnGa, the magnetic field is applied perpendicular to the surface of the trilayers. In this configuration the Hall effect can be measured simultaneously with the magnetoresistance. The extraordinary component of the Hall voltage is proportional to the magnetization and allows the measurement of hysteresis loops. The offset field of the minor hysteresis loops is a direct measure for the interlayer coupling strength.[11]

We defined 100-μm-wide Hall bars using optical lithography and wet chemical etching in a H_3PO_4:H_2O_2:H_2O 3:1:50 solution. The mask contained four staggered devices to cover the entire length of the wedge-shaped samples in one processing run. Each device consisted of a 100-μm-wide Hall bar with 12 pairs of 12-μm-wide contacts at 1-mm intervals. One sample (Mn_2Sb) was measured in the van der Pauw configuration with four-point resistance measurements[33] on 4×4 mm^2 large squares. The measurements were performed in a closed-cycle cryostat in the temperature range 9–320 K and in applied fields up to 1.5 T. As these fields are much smaller than the anisotropy field of MnGa, $\mu_0H_a=6.4$ T,[18] the magnetization remains essentially parallel to the easy axis. Here 90° configurations are ruled out, and magnetization reversal occurs through domain wall motion. In order to translate the coupling fields to the coupling energies, we have measured the magnetization of a

selected number of samples using a Princeton model 2900 alternating gradient force magnetometer (AGFM).

III. GROWTH AND STRUCTURAL PROPERTIES

For the growth of MnGa, we followed the procedure described by M. Tanaka *et al.*[20] After the growth of a 100-nm-thick GaAs buffer, the substrate was cooled down to $T_{sub} \leqslant 20\,^{\circ}C$ and an amorphous layer consisting of five alternating monolayers Mn-Ga-Mn-Ga-Mn was deposited on the GaAs $c(4\times4)$ reconstructed surface. The substrate temperature was then increased to 150–180 °C, where the amorphous layer transformed into a crystalline MnGa template and, further, to 230 °C. At this temperature the growth of MnGa is continued by coevaporation of Mn and Ga at a rate of 60 nm/h until the desired thickness was achieved.

MnGa thin films can be grown in a wide composition range from 50 to 72 at. % Mn by controlling the flux ratio, after calibration against AES and electron probe microanalysis (EPMA) measurements. The coercivity depends on the composition[21] and on the thermal treatment[34] after the film has been completed. This property was used to obtain hysteresis loops with two separate steps. The first MnGa film (soft film) was grown with the composition resulting in the lowest coercive field ($Mn_{54}Ga_{46}$) and was annealed at 300–350 °C during 10 min to reduce the coercive field even further.[21,34] The second MnGa film (hard film) was grown slightly off the ideal composition ($Mn_{60}Ga_{40}$) and annealed at 270–320 °C during 5 min to create a square hysteresis loop, but maintaining a larger coercivity.

RHEED and AES measurements have indicated some As absorption on the MnGa surface in an As-rich environment, creating a surface layer with Mn_2As-like symmetry.[35] To prevent its formation in trilayers with Mn_2Sb or GaAs spacer layers, we have preannealed the GaAs buffer layers at 430–470 °C during 10 min before the growth of the MnGa films.

Mn_2As or Mn_2Sb spacer layers were grown using a flux ratio Mn:As_2(Sb_4) of 1:3. Growth was initiated by simply opening both shutters simultaneously at a substrate temperature of $T_{sub}=250-300\,^{\circ}C$ (Mn_2As) and 170 °C (Mn_2Sb). The growth rate was 80 nm/h. The similarities between the crystal structures of Mn_2As (Mn_2Sb) and MnGa result in very good structural quality for the Mn_2As and Mn_2Sb spacer layers as is shown by RHEED and XRD measurements. *In situ* AES measurements indicated that the interfaces are abrupt without interdiffusion.[35]

GaAs spacer layers have been grown according to the procedure reported earlier, which includes coevaporation of Ga and As_2 with a flux ratio of 1:2.[13] A reduced growth temperature of $T_{sub}=210\,^{\circ}C$ and an increased growth rate of 75 nm/h compared to 300 °C and 12 nm/h in our initial work[11] were used to suppress the diffusion of Mn from the first MnGa film into the GaAs spacer. This diffusion is driven by the strong affinity between Mn and As compared to the Ga-As bond.[36–38] *In situ* AES measurements of the Mn peak as function of the GaAs spacer layer thickness showed a signal that decayed with a characteristic length [9 Å or 3.2 monolayers (ML) for the sample presented here] that is similar to the AES probing depth (typically 10–30 Å) (Ref. 39)

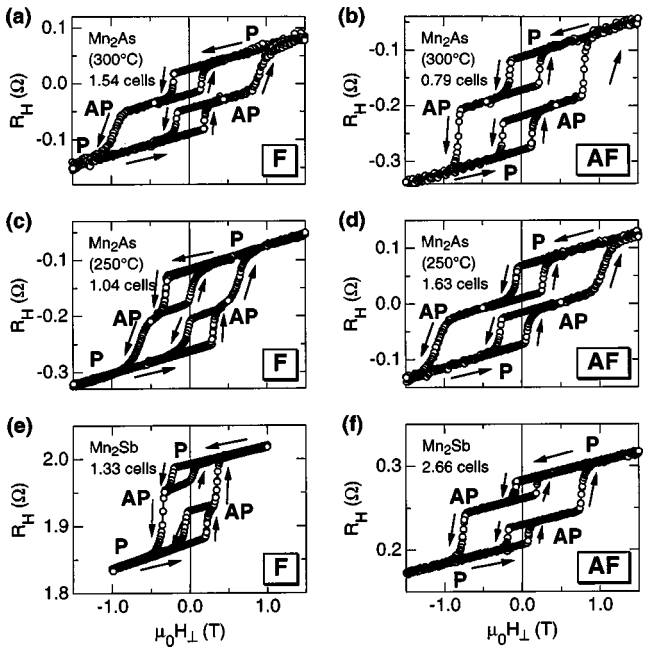

FIG. 3. Extraordinary Hall effect (EHE) hysteresis loops at $T=9$ K for trilayers with different spacer layers: (a), (b) Mn_2As grown at 300 °C, (c), (d) Mn_2As grown at 250 °C, and (e), (f) Mn_2Sb grown at 170 °C. The spacer layer thickness is indicated in number of unit cells (Mn_2As: 1 cell=0.627 nm; Mn_2Sb: 1 cell=0.656 nm). The direction of the field sweep is indicated by arrows. The labels P and AP indicate regions where the magnetizations of both MnGa films are oriented parallel and antiparallel to each other, the labels F and AF indicate samples with ferromagnetic and antiferromagnetic coupling (i.e., samples where the preferred direction of the magnetizations is P or AP).

and dropped below our detection limit (~4 at. %) at a thickness $t_{GaAs} \geqslant 12$ ML (34 Å). Here 1 ML is defined as one Ga+As layer, with a thickness 1 ML=$a_{GaAs}/2=0.283$ nm (see Fig. 1). This signal could be attributed to the buried MnGa film, indicating that there was no Mn diffusion into the GaAs spacer layer. RHEED images showed some roughening of the surface, but the decay of the AES signal confirmed that the GaAs layers were continuous without any pinholes that could lead to direct magnetic coupling between both MnGa films. The RHEED images also confirmed the zinc-blende crystal structure of the GaAs spacers. Although the low growth temperature and As_2 flux caused twinning and a deterioration of the surface morphology for thick layers, the quality in the 0–12 ML range remained sufficient for the growth of single-crystalline MnGa films on top of the spacer.

IV. MAGNETIC PROPERTIES

A. Interlayer coupling: Mn_2As and Mn_2Sb spacer layers

1. Definitions and analysis technique

The magnetic properties have been determined from extraordinary Hall effect hysteresis loops, according to the procedure described in our earlier publication.[11] Figure 3 shows typical hysteresis loops for three different spacer layers

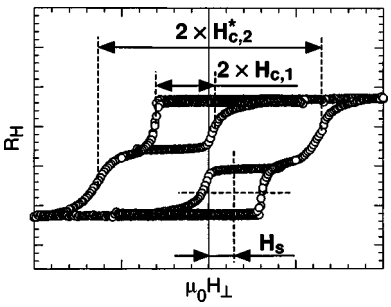

FIG. 4. Definition of the coupling field H_s, the coercive field H_{c1} of the minor loops (i.e., the soft magnetic film), and the apparent coercive field H_{c2}^* of the hard magnetic film.

(Mn_2As grown at 250 and 300 °C, and Mn_2Sb). Figure 4 shows the definitions of the coupling field H_s, the coercive field of the soft magnetic film, H_{c1}, and the apparent coercive field of the hard magnetic film, H_{c2}^*. Because of the different coercivity of both MnGa films, hysteresis loops with two steps are observed. By reversing the field sweep in between both steps, minor loops can be traced where the magnetization of the softer film is cycled without affecting the magnetization of the hard film. Interlayer coupling causes a shift of the minor loops along the field axis depending on the magnetization of the hard film, without affecting the width of the minor loops. Minor loops taken on the upper and lower branches of the overall hysteresis loop, i.e., for the two possible directions of the magnetization of the hard film, are shifted over equal fields, but in opposite directions. The field H_s (Fig. 4) over which the loops are shifted is a direct measure for the interlayer coupling strength $J=\mu_0 H_s M_1 t_1$, where M_1 and t_1 are the saturation magnetization and layer thickness of the soft magnetic film. M_1 has been measured by AGFM on a selected number of pieces cut from each wedge. We obtained about 400 kA/m for all samples, which is close to the bulk magnetization. We define the sign of H_s and J such that positive values indicate ferromagnetic coupling, as is the case for the example shown in Fig. 4. The shift of the minor loops allows us to measure both F and AF coupling quantitatively.

This technique breaks down when the F coupling becomes so large that the two steps in the hysteresis loop overlap and the hard film starts to reverse before the reversal of the soft film is complete. The curve in Fig. 3(e) is on the edge of this breakdown. In this case we have tried to estimate the coupling strength from the position of the second step H_{c2}^* of the major hysteresis loop. As can be seen from Fig. 3, this field is not constant for a given wedge-shaped sample. It is related to the actual coercive field H_{c2} by $H_{c2}^*=H_{c2}-J/(\mu_0 M_2 t_2)$, where the index 2 refers to the second (=hard) MnGa film. Since we do not have access to the intrinsic value of H_{c2}, we cannot determine J directly from H_{c2}^*. However, as each wedge-shaped sample represents only one growth run, H_{c2}, M_2, and t_2 are constant over the entire sample. This allowed us to fit J vs H_{c2}^* in the range where both could be measured and extrapolate this relationship to the regions where J could not be measured directly. Data points that have been obtained in this way are represented by shaded circles in Figs. 6(a) and 11(a).

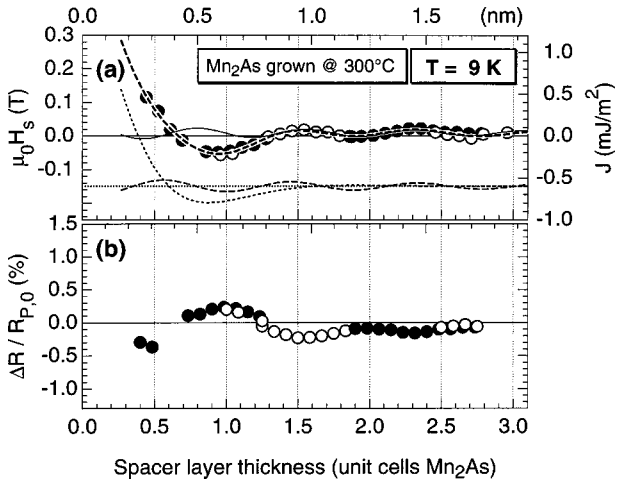

FIG. 5. Spacer layer thickness dependence of the magnetic properties of a $\{10\,\mathrm{nm}\,Mn_{54}Ga_{46}/Mn_2As/8\,\mathrm{nm}\,Mn_{60}Ga_{40}\}$ trilayer with wedge-shaped Mn_2As spacer layer grown at 300 °C. The measurements are taken at 9 K. Solid and open circles differentiate the four Hall bar devices that were used to cover the entire spacer layer wedge. (a) Interlayer coupling field H_s and coupling strength J. Solid and thick dashed lines are best fits using one and two decaying sine functions, respectively. Thin dashed and dotted lines are the individual terms of the two-component fit, offset vertically for clarity. (b) Magnetoresistance $\Delta R/R_{P,0}=(R_P-R_{AP})/R_{P,0}$, where the subscripts P (AP) indicate parallel (antiparallel) orientation of the magnetization directions of both MnGa films.

The dependence of the interlayer coupling strength J on the spacer layer thickness d has been fitted to exponentially decaying since functions of the form

$$J(d)=J_0+\sum_{i=1}^{N} J_i \sin[2\pi(d-d_i)/P_i]\exp(-d/\lambda_i), \quad (1)$$

where P_i are the oscillation periods, λ_i the decay lengths, and the number of terms $N=1$ or 2. In the framework of the quantum interference model for nonmagnetic spacers by Bruno,[6] this would indicate the contributions of one or two critical (that is, stationary) spanning vectors on the Fermi surface of the spacer layer. Since this model predicts a d^{-2}-like envelope for metallic spacer layers, we have also attempted d^{-2}- and d^{-n}-like decaying sines; however, we consistently found that an exponential decay gave the best results.

2. Mn_2As and Mn_2Sb spacer layers

The spacer layer thickness dependence of the IEC at $T=9$ K for two Mn_2As spacer layers grown at different substrate temperatures is shown in Figs. 5 and 6. The spacer layer grown at the optimum growth temperature (300 °C) clearly shows two oscillatory components in the thickness dependence of the IEC, Fig. 5(a). The main component is a short-period oscillation with $P_1=5.5$ Å (0.88 structural unit cells of Mn_2As) and a long decay length $\lambda_1=18$ Å. At small spacer layer thicknesses, it is superimposed on a quickly decaying component with $P_2=12.8$ Å and $\lambda_2=2.3$ Å. The pe-

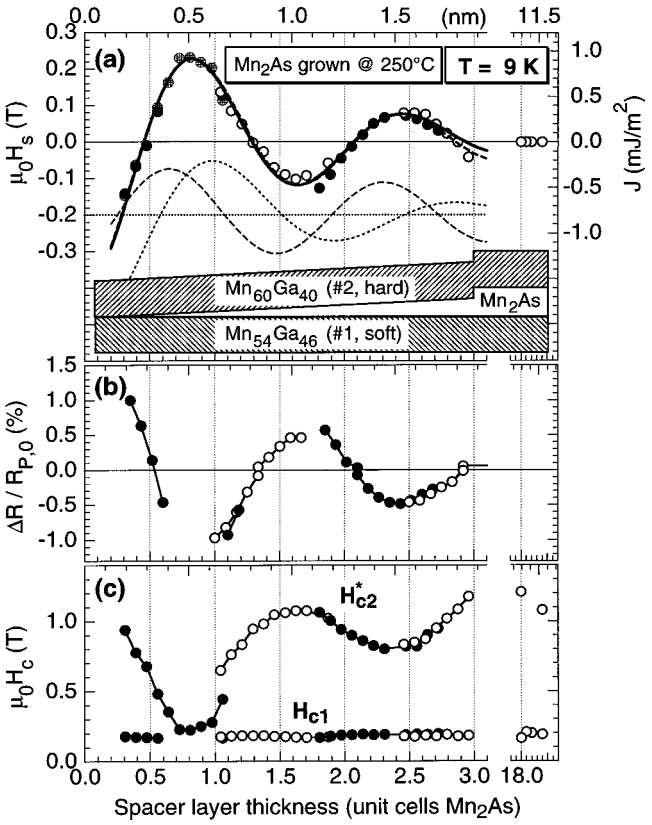

FIG. 6. (a), (b) Same as Fig. 5, for a Mn_2As spacer layer grown at 250 °C. Shaded circles in (a) are values estimated from H_{c2}^*, not determined from the shift of the minor loops. The inset in (a) shows the sample structure with the soft $Mn_{54}Ga_{46}$ (No. 1) and hard $Mn_{60}Ga_{40}$ films (No. 2) at the bottom and top, respectively. (c) Coercive field H_{c1} of the minor loop (film No. 1) and position H_{c2}^* of the second step of the overall hysteresis loop (apparent coercive field of film No. 2).

riods remain unchanged at $T=300$ K, but the decay length λ_1 is shorter (Table I). (The variations in P_2 and λ_2 are believed to be not significant: because of the extremely fast decay, small measurement errors have a large impact on these values.)

The Mn_2As spacer layer grown at 250 °C (at the lower end of the growth window for Mn_2As) shows a stronger coupling, but with only one oscillatory component with $P_1=10.2$ Å (1.6 unit cells) and decay length $\lambda_1=8.8$ Å (1.4 unit cells), as indicated by the thick solid line in Fig. 6(a). The temperature dependence of the coupling suggests the presence of an additional term (see below); hence, we have fitted to the sum of two decaying sines as well (thick dashed line). The results are summarized in Table I. The fit returns two components with nearly equal period listed in Table I and shown by the offset curves in Fig. 6(a). However, the overall accuracy of the fit does not improve except possibly at the thick end of the spacer layer (3 unit cells of Mn_2As), and we cannot be sure that this result is significant. The different thickness dependence of the spacer layer grown at 250 °C is presumably due to a lower crystal quality. The film is grown at the lower end of the growth window of Mn_2As. Thick layers show increased surface roughness and small shoulders on the main XRD peaks that may be the result of nonstoichiometric growth (e.g., As interstitials or antisite defects). Since this may influence the electronic properties of the material, we will base our further analysis exclusively on the Mn_2As spacer grown at 300 °C.

The results for a Mn_2Sb spacer layer with a similar crystal lattice but a different magnetic structure are shown in Fig. 7. For reasons we will discuss below, we have fitted only the measurements taken at room temperature. We obtain two periods that are about 50% longer than their counterparts in the highest-quality Mn_2As film grown at 300 °C. Their relative strength and decay periods are inverted, with the long-

TABLE I. Spacer layer material (with growth temperature), measurement temperature, periods P_i, and decay lengths λ_i of the thickness oscillations of the coupling, relative goodness of fit χ_2^2/χ_1^2, and orientation of the moments in the spacer layer for the $\{10\text{ nm }Mn_{54}Ga_{46}/\text{spacer}/8\text{ nm }Mn_{60}Ga_{40}\}$ trilayers under study. Periods and decay lengths are given both in Å and in the number of unit cells of Mn_2As (6.27 Å) and Mn_2Sb (6.56 Å) or in the number of monolayers of GaAs (2.83 Å). The dominating contributions are indicated in boldface. For Mn_2Sb no low-temperature values are listed since the effect of the spin reorientation transition is superimposed on the normal thickness dependence. The relative goodness of fit shows the ratio of the χ^2 values of the two-component fit to the single component fit.

Spacer layer (growth T)	Temperature (K)	P_1 [Å (cells)]	λ_1 [Å (cells)]	P_2 [Å (cells)]	λ_2 [Å (cells)]	χ_2^2/χ_1^2	Moments
Mn_2As (300 °C)	9	**5.5 (0.88)**	**17.7 (2.82)**	12.8 (2.04)	2.3 (0.37)	0.20	Basal plane
	300	**5.5 (0.88)**	**11.0 (1.76)**	11.0 (1.76)	3.2 (0.51)		Basal plane
Mn_2As (250 °C)	9			10.2 (1.63)	8.8 (1.40)	0.91	Basal plane
One component	250			10.3 (1.65)	12.2 (1.95)		Basal plane
Mn_2As (250 °C)	9	10.3 (1.65)	30.1 (4.80)	11.8 (1.88)	8.03 (1.28)	0.91	Basal plane
Two components	250	11.1 (1.77)	∞ (∞)	13.3 (2.11)	18.9 (3.01)		Basal plane
Mn_2Sb (170 °C)	9	–	–	–	–	0.02	Reorients
	300	8.2 (1.25)	7.7 (1.18)	**17.6 (2.68)**	**14.4 (2.19)**		c axis
GaAs (210 °C)	9	**9.1 (3.21)**	**4.7 (1.65)**	58.2 (20.6)	2.9 (1.02)	0.74	–
	300	**7.4 (2.60)**	**5.7 (2.02)**	13.9 (4.91)	4.7 (1.68)		–

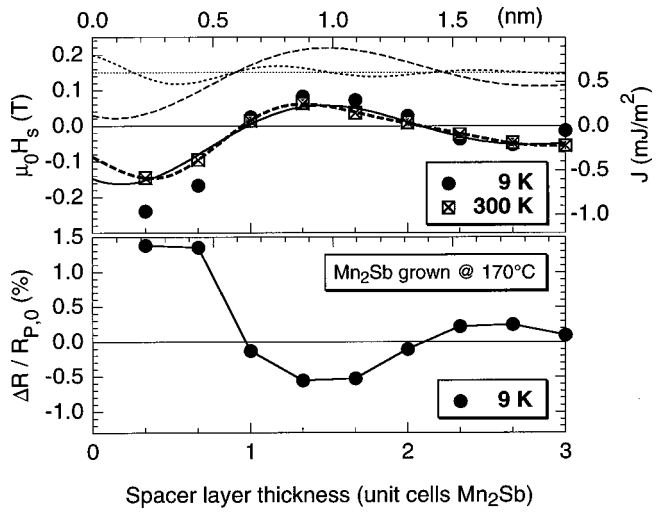

FIG. 7. Same as Fig. 5, for a Mn_2Sb spacer layer grown at 170 °C. The measurements were performed on van der Pauw squares of 4×4 mm^2 at $T=9$ K and 300 K. Fitting is done to the data taken at $T=300$ K.

period oscillation now making the dominating contribution.

Comparing Mn_2As ($T_{sub}=300$ °C) with Mn_2Sb, it is clear that the dependence of the interlayer coupling strength on the spacer layer thickness does not represent the bulk magnetic structure of the spacer layers. The behavior of both materials is similar, with the periods for Mn_2Sb shifted towards longer wavelengths. In fact, the dominating component is opposite from what the long-range magnetic order of the spacer layers would suggest. Mn_2As with a large magnetic period of 2 structural unit cells shows a strong short-period component $\lambda_1\approx0.9$ unit cells, whereas Mn_2Sb with a magnetic period of 1 unit cell has a stronger long period component $\lambda_2\approx2.7$ unit cells.

The absence of a correlation with the magnetic period of the spacer layer and the similarity of the periods to those obtained for many nonmagnetic transition-metal spacers[3] suggests that the coupling is simply caused by quantum interference effects in the spacer layer as for nonmagnetic spacers.[6,40]

The temperature dependence of the interlayer coupling strength through Mn_2As spacer layers grown at 300 and 250 °C is shown in Figs. 8 and 9. In both cases we find a

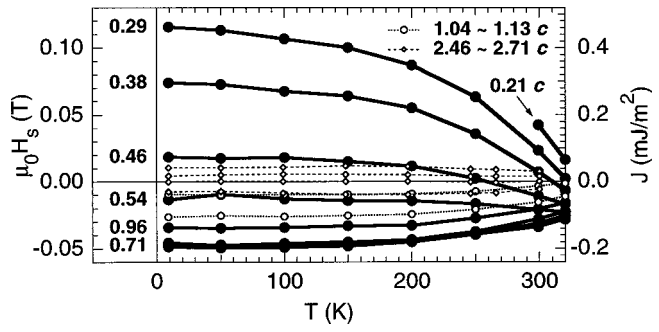

FIG. 8. Temperature dependence of the coupling strength through a Mn_2As spacer layer grown at 300 °C. The labels indicate the spacer layer thickness in unit cells of Mn_2As (= 0.627 nm).

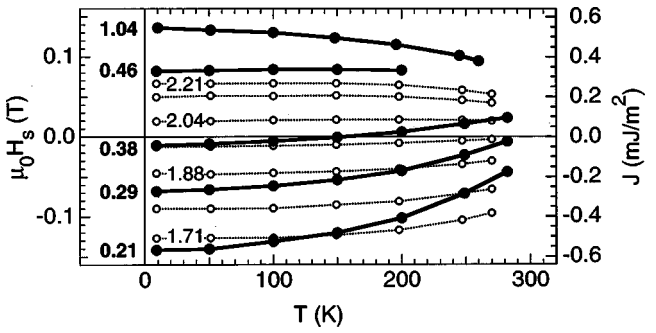

FIG. 9. Temperature dependence of the coupling strength through a Mn_2As spacer layer grown at 250 °C. The labels indicate the spacer layer thickness in unit cells of Mn_2As (=0.627 nm).

strong negative temperature coefficient for spacer layer thicknesses below 1 structural unit cell and a much weaker negative temperature dependence for larger thicknesses. For particular cases where the two oscillatory components have opposite signs, we observe a sign reversal of the coupling. This suggests that both components have a different temperature dependence (that is, a different critical temperature at which the coupling vanishes).

Mn_2Sb spacer layers thinner than approximately 2 unit cells show a behavior similar to Mn_2As, with a negative temperature coefficient that is strongest at small spacer layer thicknesses (Fig. 10). However, for thicknesses exceeding 2 unit cells (thick lines), the temperature dependence is more complicated. The interlayer coupling is quenched at low temperature, with a transition temperature T_{max} that increases with increasing spacer layer thickness from $T_{max}\approx180$ K at $d_{Mn_2Sb}=2.33$ unit cells to $T_{max}\approx250$ K at $d_{Mn_2Sb}=3$ unit cells (see Fig. 10, inset).

This is the expected behavior if the Mn_2Sb spacer layer undergoes the spin reorientation transition outlined in Fig. 2. Above the transition temperature the spins are parallel to the

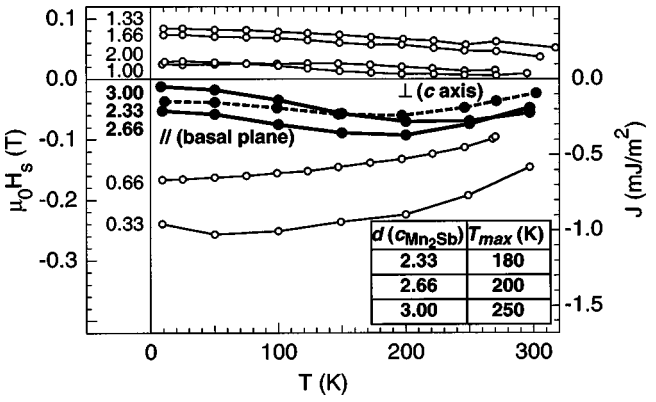

FIG. 10. Temperature dependence of the coupling strength through a Mn_2Sb spacer layer grown at 170 °C. The labels at the left side indicate the spacer layer thickness in unit cells of Mn_2Sb (=0.656 nm). Thick lines show spacers with thickness larger than 2.33 unit cells where the coupling strength is quenched below a critical temperature T_{max}, a possible indication of the spin reorientation transition. The inset lists the approximate value of T_{max} as function of the spacer layer thickness.

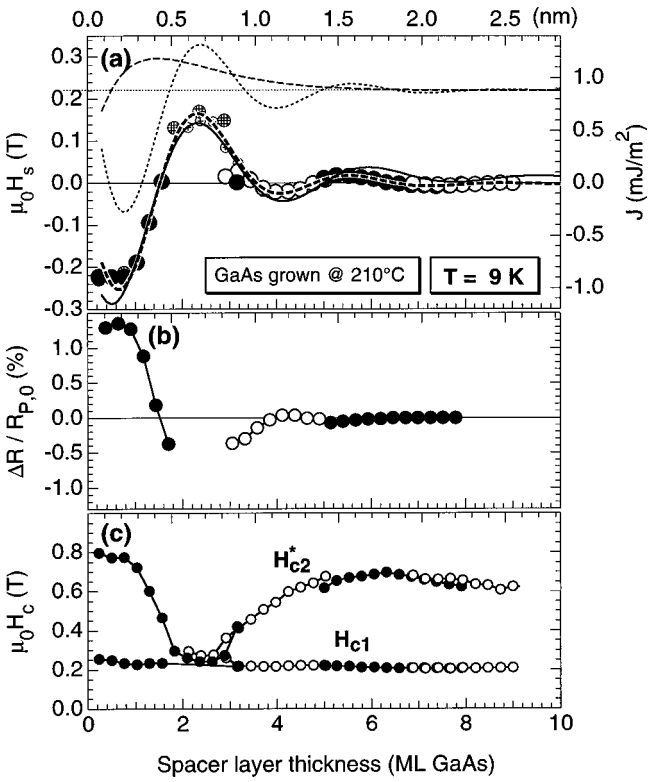

FIG. 11. Same as Fig. 5, for a GaAs spacer layer grown at 210 °C.

MnGa spins, and a strong interaction is expected. Below the transition temperature the spins are orthogonal to MnGa and a suppression of the coupling strength can be expected. The fact that the spin reorientation transition is not observed for spacer layer thicknesses less than 2 unit cells can be attributed to induced perpendicular anisotropy caused by the adjacent MnGa films, keeping the Mn_2Sb moments parallel to the *c* axis at all temperatures.

In other words, at $T=300$ K the Mn_2Sb spins are parallel to the *c* axis (the bulk easy axis at that temperature) for all spacer layer thicknesses, while at low temperatures the moments are parallel to the *c* axis for $d_{Mn_2Sb} \leqslant 2$ unit cells but orthogonal to *c* for $d_{Mn_2Sb} > 2$ unit cells. As the relative orientation of the quantization axes changes as a function of the spacer layer thickness, the thickness dependence of the interlayer coupling at 9 K (Fig. 7) could not be fitted to Eq. (1).

3. GaAs spacer layers

The thickness and temperature dependence of the interlayer coupling for a GaAs spacer layer without detectable Mn content (decay length for the Mn signal in AES measurements of 9 Å or 3.2 ML) grown at $T_{sub}=210$ °C is shown in Figs. 11(a) and 12. In spite of the suppressed Mn contamination, we still find an oscillatory thickness dependence with a period of $P_1=9.1$ Å. The coupling strength at low spacer layer thicknesses is comparable to the Mn_2As and Mn_2Sb cases but it decays much faster with increasing thickness, with $\lambda_1=4.7$ Å. Again, this is superimposed on a second

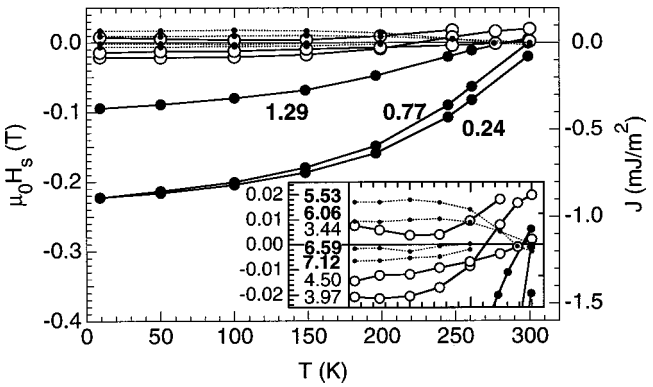

FIG. 12. Temperature dependence of the coupling strength through a GaAs spacer layer grown at 210 °C. The labels indicate the spacer layer thicknesses in monolayers of GaAs (1 ML GaAs=0.283 nm). The region $-25\ \text{mT} \leqslant \mu_0 H_s \leqslant 25\ \text{mT}$ is shown expanded in the inset.

component with even shorter decay length λ_2. The period P_2 is long and could not be determined exactly because of the fast decay.

The temperature dependence as well is similar to Mn_2As and Mn_2Sb, with a negative temperature coefficient and sign reversals for certain spacer layer thicknesses, suggesting a different critical temperature for the two components of the coupling.

B. Magnetoresistance

Figure 13 shows typical magnetoresistance measurements for the three different metallic spacer layers discussed above. The curves have been normalized to the resistance at zero applied field with parallel orientation of the magnetizations of both MnGa films $R_{P,0}=R_P(\mu_0 H_{appl}=0\ \text{T})$. The most striking feature is the correlation of the sign of the magnetoresistance $\Delta R=(R_P-R_{AP})$ with the sign of the interlayer coupling, where R_P and R_{AP} are the resistances with the magnetizations of both MnGa films parallel and antiparallel to each other, respectively. Samples with ferromagnetic interlayer coupling [Figs. 13(a), 13(c), and 13(e)] show the highest resistance when both magnetizations are aligned antiparallel to each other ($R_{AP}>R_P$), as would be expected in the normal GMR case. Samples with antiferromagnetic coupling [Figs. 13(b) 13(d), and 13(f)], however, show the opposite behavior with a lower resistance when the magnetizations are aligned antiparallel ($R_{AP}<R_P$).

The correlation with the interlayer coupling *J* is shown more clearly in Figs. 5, 6, 7, and 10 where we compare the thickness dependence of $\Delta R/R_{P,0}$ and *J*. Here we have taken ΔR as the constant resistance difference (R_P-R_{AP}) for those samples with an extended AP region such as Figs. 13(a), 13(b), 13(d), 13(f) or the largest value of (R_P-R_{AP}) for samples where the AP region is very narrow, as in Figs. 13(c) and 13(e). The results at $T=9$ K are summarized in Fig. 14(a). The data points for all samples fall on one universal straight line through the origin, irrespective of the spacer layer material. The five outliers slightly above the general curve are all for very small spacer layer thicknesses

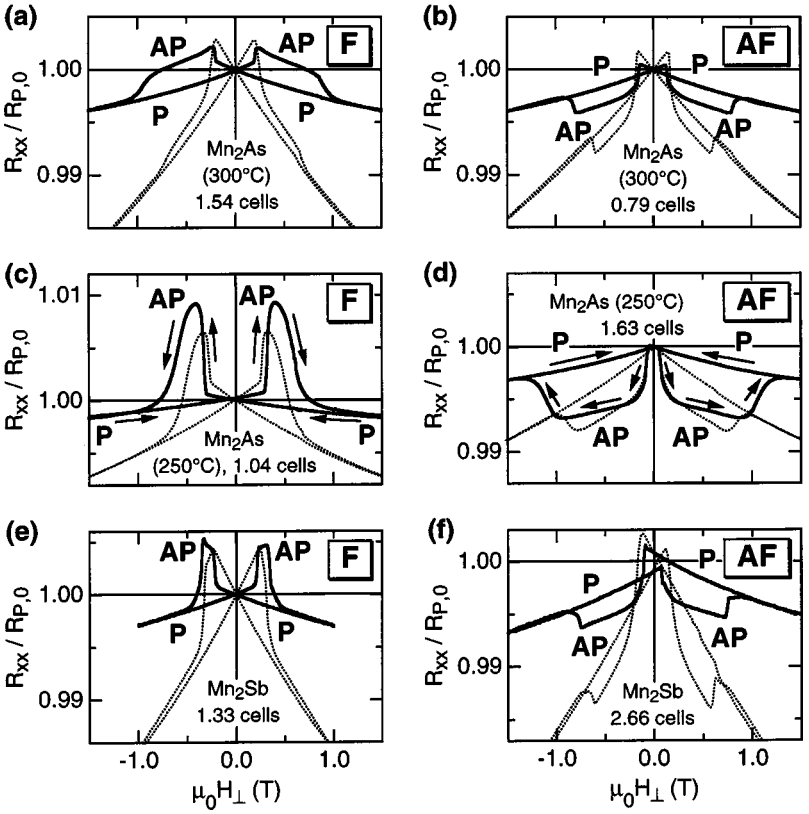

FIG. 13. Magnetoresistance curves at $T=9$ K (solid lines) and room temperature (dotted curves) for the same samples as shown in Fig. 3. Only the major hysteresis loops are shown. The arrows indicate the direction of the field sweep. The curves are normalized to the resistance for parallel magnetizations at zero applied field $R_{\mathrm{P},0}$.

where the variations of ΔR and J vs the spacer layer thickness are largest and most nonlinear and where phase shift errors between ΔR and J are most likely to occur, as will be discussed below.

Figure 14(b) shows the relation between $\Delta R/R_{\mathrm{P},0}$ and J at room temperature, together with the paths traced by a selected number of devices at intermediate temperatures. Most of the points stay close to the same center line, even for the Mn_2Sb spacer layer when it goes through the spin reorientation transition (dotted lines with arrows). The increased scatter in the data points can partly be attributed to increased uncertainty on the ΔR measurements due to a narrowing of the plateaus caused by the decreasing coercive fields H_{c1} and H_{c2} at higher temperatures, and to the increased interference of the ''butterfly''-shaped features in the resistance around magnetization reversal,[41] leading to uncertainties up to 0.1%–0.2% in $\Delta R/R_{\mathrm{P},0}$. Only the data points for the GaAs spacer layer at very small thickness show a different behavior, with $\Delta R/R_{\mathrm{P},0}$ remaining approximately 1% while the coupling J vanishes.

For the measurements taken in the Hall bar configuration (Figs. 5, 6, and 10), it has been necessary to correct for a phase error between the measured values of ΔR and J, as shown in Fig. 15. Because of the wedge shape of the spacer layer, the Hall resistance $R_H(x)\,[\Omega]$ and the forward resistivity $\mathcal{R}_{xx}(x)\,[\Omega/\mathrm{cm}]$ vary continuously as a function of the position x along the Hall bar. Whereas the R_H loops (and thus the coupling field H_s and the coupling energy J) are measured locally at positions x_N and x_{N+1}, this is not the case for the $\mathcal{R}_{xx}$ loops. Rather, the measurement returns a resistance $R_{xx}(x_N,x_{N+1})\,[\Omega]$, which is the integration of $\mathcal{R}_{xx}$ between x_N and x_{N+1}. If the variation of $\mathcal{R}_{xx}$ with x is slow, we can use a linear approximation

$$\begin{aligned} R_{xx}(x_N,x_{N+1}) &= \int_{x_N}^{x_{N+1}} \mathcal{R}_{xx}(x)\,dx \\ &\approx \mathcal{R}_{xx}\left(x=\frac{x_N+x_{N+1}}{2}\right)(x_{N+1}-x_N) \\ &\propto \mathcal{R}_{xx}\left(x=\frac{x_N+x_{N+1}}{2}\right), \end{aligned} \tag{2}$$

showing that the measured R_{xx} is proportional to $\mathcal{R}_{xx}$ at position $(x_N+x_{N+1})/2$. In Figs. 5, 6, and 10, we have plotted the $\Delta R/R_{\mathrm{P},0}$ values at x positions halfway between the J values. In Fig. 14 we have compared $\Delta R/R_{\mathrm{P},0}$ with interpolated values of the coupling J, which are given in linear approximation by

$$R_H\left(x=\frac{x_N+x_{N+1}}{2}\right)\approx\frac{R_H(x=x_N)+R_H(x=x_{N+1})}{2}, \tag{3a}$$

$$J\left(x=\frac{x_N+x_{N+1}}{2}\right)\approx\frac{J(x=x_N)+J(x=x_{N+1})}{2}. \tag{3b}$$

Our data [Fig. 14(a)] show that this procedure generally has yielded good results. Only in the regions with very fast variation of coupling strength and (magneto)resistance vs the spacer layer thickness do some errors due to a phase shift become apparent. The above corrections were not applied to

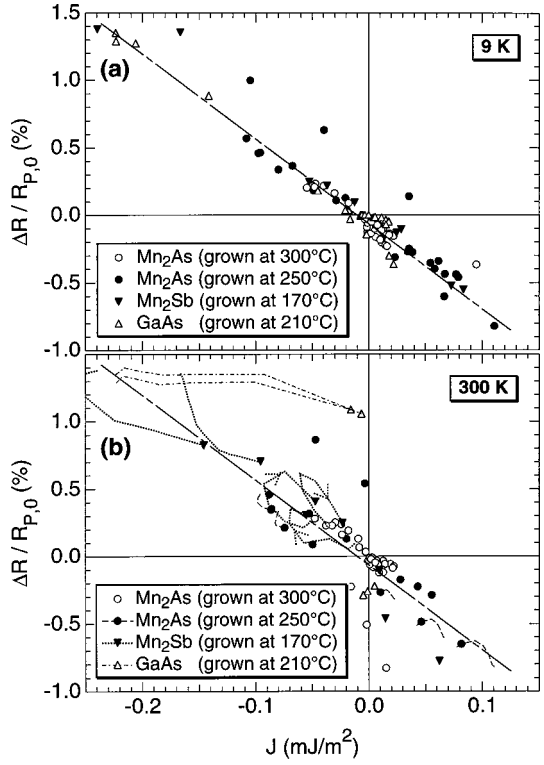

FIG. 14. Correlation between the magnetoresistance $\Delta R/R_{P,0}=(R_P-R_{AP})/R_{P,0}$ and the interlayer coupling strength J for $\{10\ \mathrm{nm}\ Mn_{54}Ga_{46}/\mathrm{spacer}/8\ \mathrm{nm}\ Mn_{60}Ga_{40}\}$ trilayers with different spacer layer materials. (a) $T=9$ K, (b) $T=300$ K, with traces from 9 to 300 K for selected data points. Dotted lines with arrows represent thick Mn_2Sb spacer layers that go through the spin reorientation transition.

the Mn_2Sb film which was measured in the Van der Pauw configuration on $4\times4\ \mathrm{mm}^2$ large squares.

The magnetoresistance loops R_{xx} vs applied field $\mu_0 H_{\mathrm{appl}}$ (Fig. 13) show one additional feature, namely, a negative background which is typical for magnetic metals.[42] It is caused by forced magnetization when the external field reduces the thermally induced disorder in the magnetic moments and thereby reduces the scattering. Usually, this effect vanishes at low temperatures when there is no thermally induced disorder, leaving the positive magnetoresistance due to the Lorentz force which is also found in nonmagnetic metals. The background magnetoresistance of the MnGa-based trilayers is nearly linear in applied fields up to 1.5 T, with sample-dependent slopes ranging from -0.1%/T to -0.4%/T at 9 K and from -0.6%/T to -1.7%/T at 300 K. Surprisingly, the background is still negative at 9 K. This is an indication that there is additional, nonthermally induced, disorder in the alignment of the moments. One possible origin is the chemical disorder with antisite defects caused by the nonstoichiometric composition and by the relatively low growth temperature.[34] The chemical disorder also manifests itself in the alloy scattering, resulting in a residual resistivity at 9 K of about 40% of the room-temperature resistivity.

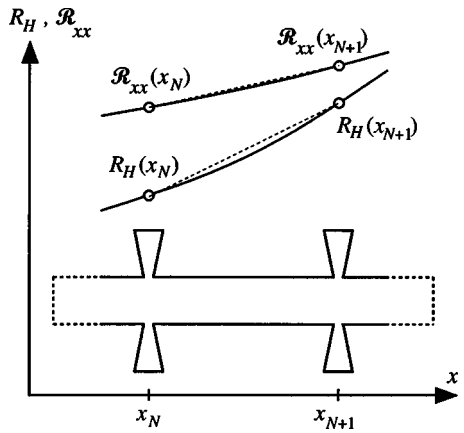

FIG. 15. Schematic view of the local forward resistance $\mathcal{R}_{xx}$ and the Hall resistance R_H along the sample. The measured forward resistance $R_{xx}(x_N,x_{N+1})$ is the (nonlocal) integration of $\mathcal{R}_{xx}$ between positions $x=x_N$ and $x=x_{N+1}$.

V. DISCUSSION

A. Interlayer coupling and the magnetic structure of the spacer layer

At first glance it seems as if the thickness and temperature dependences of the interlayer coupling lead to opposite conclusions: on the one hand, we find that the thickness dependence is not related to the magnetic structure of the spacer layer, while the temperature dependence for Mn_2Sb suggests otherwise. However, the contradiction is only apparent, as the two effects are related to different physical origins.

Bruno has given an extensive treatment of the interlayer coupling through *nonmagnetic* spacer layers, based on a description in terms of quantum interferences.[6] He showed that the thickness dependence of the coupling (the oscillation period) is determined by the complex Fermi surface of the spacer layer, while the magnitude and phase of the coupling are mainly determined by the reflection coefficients at the ferromagnet–normal-metal interfaces and depend only to a lesser extent on the Fermi surface. Although the formalism used in this work is strictly speaking not valid for spacer layers with long-range magnetic order, quantum-size effects are expected to remain present, but superimposed on them there may be the influence of the magnetic order of the spacer layer. Since we did not observe any signature of the (bulk) long-range order of the Mn_2As and Mn_2Sb spacer layers, we will discuss our results in terms of the general conclusions of Bruno and show that they are in qualitative agreement with them.

First, we look at the thickness dependence of the coupling. Chonan *et al.*[43] have compared the band structures of various Cu_2Sb-type compounds in the paramagnetic state. They found four families with different topologies for the Fermi surface. Mn_2As and Mn_2Sb belonged to the same family and have similar Fermi surfaces, consisting of a hole surface around the Γ point and two complicated electron surfaces. Hence the similarity of the thickness dependence of the coupling (two oscillation periods with the same ratio $P_1/P_2\approx2$, Table I) is not surprising in the framework of the quantum interference model. It is worthwhile to mention that there also exist band structure calculations in the magnetic

states of Mn_2As and Mn_2Sb by Yang *et al.*[24] and Wijngaard *et al.*,[30] respectively. However, it is difficult to make quantitative predictions of the interlayer coupling from these results.

We do not have a clear answer to the question why the long-range order of the spacer layer material is not reflected in the oscillation periods of the coupling. One conceivable reason could be an orthogonal orientation of the spins in the ferromagnetic films (*c* axis) and the spacer layer (basal plane). However, we can rule out this possibility since it would be inconsistent with the results for the Mn_2Sb spacer at room temperature where all quantization axes are parallel and where we still do not observe the magnetic structure of the spacer layer in the thickness dependence.

The most likely explanation for the absence of any sign of the (bulk) magnetic order in the oscillation periods is a modification or quenching of the order caused by the small thickness of the spacer layers. The energy differences between the various magnetic structures found in the Cu_2Sb-type compounds are relatively small as is indicated by the wide variety of structures as a function of the composition and lattice constant. For example, in the case of $Mn_{2-x}Cr_xSb$ with $x=0.023$ and $x=0.03$ the existence of a weakly ferrimagnetic third state with magnetic period $3c_{Mn_2Sb}$ has been reported as an intermediate state between the ferrimagnetic state at high temperature and the antiferromagnetic state at low temperature.[27,44,45] It is therefore very well possible that the magnetic order in our ultrathin spacers is altered from the bulk configuration or even becomes commensurate with the quantum-size oscillations in the interlayer coupling.

Next, we address the question why the spin reorientation transition of Mn_2Sb still has an influence on the strength of the interlayer coupling, even when the long-range order is modified or quenched. The magnetocrystalline anisotropy (MCA) originates from the spin-orbit interaction. This is a local energy term for each individual moment which does not depend on the orientation of the neighboring moments. It is not influenced by the exchange interaction between neighbors which is responsible for the long-range order. As a result, the preferential axis along which the moments align is unrelated to the nature and period of the long-range order or even to its presence or absence.[46]

Consequently, the spin reorientation transition of Mn_2Sb is expected to persist unchanged even when the long-range order is modified, and hence it may influence the reflection coefficients at the interfaces. When the moments of the spacer layer are in the basal plane, orthogonal to the MnGa moments (e.g., thick Mn_2Sb spacers at low temperature), each spin-up or spin-down electron of MnGa is decomposed in a combination of spin ''left'' and spin ''right'' in the spacer layer, and couples to both spin subbands at the same time. This is illustrated in Fig. 16(b) for parallel alignment of both MnGa films. The situation is clearly different when both easy axes are collinear, Fig. 16(a), when each MnGa electron couples to only one spin subband in the spacer layer. The reflection coefficients can be expected to differ in both cases, and according to the quantum interference model,[6] also the coupling strengths will differ. Although this argument by itself does not predict in which configuration the coupling should be strongest, the temperature dependence for thick Mn_2Sb spacers indicates that the coupling is strongest when the Mn_2Sb moments are parallel to the *c* axis, i.e., when they are collinear with the MnGa moments.

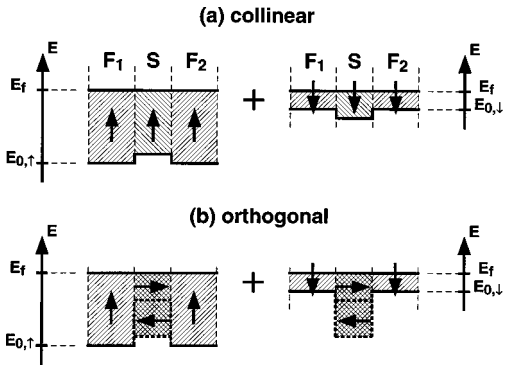

FIG. 16. Schematic band lineup for ferromagnet-spacer-ferromagnet trilayers with magnetic spacer layers, illustrating the dependence of the reflection coefficients on the relative orientation of the easy axes. The sketches are drawn for parallel orientation of both ferromagnetic films. The phase and amplitude of the interlayer coupling are determined by the reflection coefficients for spin-up (left-hand side) and spin-down (right-hand side) electrons. (a) Collinear easy axes: small reflection coefficients. (b) Orthogonal easy axes: larger reflection coefficients.

Finally, we discuss the orientation of the moments in *thin* Mn_2Sb spacer layers (where the spin reorientation transition is not observed) and in the Mn_2As spacer layers. Comparing the strength of the coupling through thin and thick Mn_2Sb spacers in Fig. 10, we see that the strength for thin spacers is similar to that of thick spacers at high temperature. I.e., the moments remain along the *c* axis and the spin reorientation transition is suppressed. This can be attributed to induced perpendicular anisotropy from the adjacent MnGa films (interface contribution), which dominates the magnetocrystalline anisotropy of the thin Mn_2Sb layer (bulk contribution) below a critical film thickness. This is in agreement with the observation that Mn_2Sb straddles the transition point from positive to negative magnetocrystalline anisotropy. Hence the absolute anisotropy values are small, and the magnetocrystalline anisotropy is easily dominated by the MnGa-induced anisotropy.

The coupling strength for the Mn_2As spacers is smaller than for Mn_2Sb ($J_{Mn_2Sb} > J_{Mn_2As,250\,°C} > J_{Mn_2As,300\,°C}$). Setting aside possible differences in quality between the various samples, this suggests that the moments in Mn_2As are in the basal plane, as in bulk Mn_2As, and that the induced perpendicular anisotropy cannot manifest itself. This can be already be understood from the general argument that Mn_2As is farther away from the spin reorientation transition (a zero crossing of the MCA) than Mn_2Sb; hence, the absolute value of the magnetocrystalline anisotropy is bound to be larger.

A more quantitative argument is based on neutron diffraction measurements on $Mn_{2-x}Cr_xSb$,[47] which have shown that the ferrimagnetic-to-antiferromagnetic transition is accompanied by a decrease in local moment on the Mn-I site and an increase in local moment on the Mn-II site. This

result is confirmed by band calculations on Mn_2As,[24] while calculations on Mn_2Sb (Ref. 30) did not show a significant change in moment. As the anisotropy energy is proportional to the local magnetic moment, the balance between the competing anisotropies on Mn-I and Mn-II sites is disturbed. Both contributions no longer cancel out, and a large net anisotropy is obtained. As the Mn-I sublattice has a positive (*c*-axis) anisotropy while Mn-II gives a negative (in plane) contribution, the overall anisotropy of the antiferromagnetic structure is strongly in plane.[26] It can therefore be expected to dominate over the induced perpendicular anisotropy from MnGa, keeping the Mn_2As moments in our samples in the basal plane over the entire thickness range under study.

B. GaAs spacers: Interlayer coupling

Although the magnetic contamination of the GaAs spacer layers has been strongly suppressed and the layers had the expected zinc-blende crystal structure, we found oscillatory thickness dependence and a negative temperature coefficient for the interlayer coupling.

The strong coupling at small spacer layer thicknesses is possibly related to the Mn_2As-like surface layer that develops on the MnGa films in an As background. The persisting oscillatory coupling at larger spacer layer thicknesses is carried by the GaAs spacer layer itself. Our analysis in the preceding paragraphs has shown that it cannot be attributed to the magnetic influence of any Mn contamination that might remain below the detection limit of AES ($\leqslant 4$ at. %). From the AES results we could also exclude the presence of pinholes.

Therefore we are forced to conclude that the GaAs spacer layers have a metallic character. Since RHEED observations have shown a zinc-blende crystal structure, this suggests a high concentration of defect levels at the band edges or inside the forbidden gap. Stacking faults and twin boundaries caused by the nucleation on a dissimilar substrate,[10] excess As related to the low-temperature growth of GaAs, and the remaining Mn impurities may all contribute to a defect band that mediates the magnetic coupling. The shorter decay lengths are in agreement with the surface roughening of the GaAs spacer, resulting in a smearing out of the oscillations.

We conclude that the growth of GaAs spacer layers with satisfactory semiconducting properties in MnGa/GaAs/MnGa trilayers is not possible, in spite of the successful work on related systems such as NiGa/GaAs and CoGa/GaAs.[10] There is no allowed growth window between Mn contamination of the spacer layer at high growth temperatures (300 °C) and insufficient crystal quality of the spacer layer at lower temperatures (210 °C).

C. Magnetoresistance

Barnas and Bruynseraede have performed calculations in a free-electron-like model and predicted a correlation between quantum-size effects in the interlayer coupling and the magnetoresistance.[15] They found an oscillatory component in the magnetoresistance that is in phase with the oscillations in the interlayer coupling and has a polarity that is in agreement with our experimental results. In general, the quantum-size oscillations in the magnetoresistance are superimposed on a background MR that decays monotonously with the spacer layer thickness. This component is the traditional giant magnetoresistance and is due to spin-polarized scattering. In the special case where the scattering is not spin dependent, the background is zero and the quantum-size oscillations give rise to sign reversals of the magnetoresistance. More recent calculations by Barnas and Bulka[48] have predicted the existence of additional periods in the magnetoresistance, related to the potential barriers at the interfaces, that have no counterpart in the interlayer coupling.

When applying this model to our magnetic spacer layers, there was initially the concern that the coupling might be of a different origin (exchange-bias effects), in which case a prediction based on quantum-size effects would be void. Our present result—that the interlayer coupling is indeed of quantum-size origin—takes away this concern. Since the model is based on a free-electron-like description, it does not explain quantitatively some of our observations. In particular, there is no *a priori* reason why all samples should show exactly the same ratio between $\Delta R/R_{P,0}$ and J as seen in Fig. 14(a), especially given the considerable variation in amplitudes and oscillation periods between the different samples. The similar nature of the Fermi surfaces of Mn_2As and Mn_2Sb in the paramagnetic state[43] could account for the same ratios for these two materials. However, the GaAs spacer layer would be expected to behave differently. Furthermore, the absence of GMR offset indicates that the scattering is spin independent, implying either that there is no spin asymmetry in the scattering in the MnGa layers or that the spin information is not transferred through the spacer layer. A more detailed description is needed to verify these observations.

The existence of a universal ratio between $\Delta R/R_{P,0}$ and J for all spacer layer materials suggests that the link between magnetoresistance and coupling is more direct than a common dependence on a third factor. This is the premise of the frustration magnetoresistance model we have proposed earlier.[12] This model is phenomenological in concept, but it takes into account a number of the peculiarities of our materials system. It is based on the observation that scattering due to magnetic disorder constitutes an important part of the resistivity of our trilayers, as indicated by the large negative background of the MR curves related to forced magnetization (Fig. 13). In the same way as an external field, the interlayer coupling can promote or counteract the alignment or disorder *within* the MnGa films. When the magnetic alignment [parallel (P) or antiparallel (AP)] of both MnGa films is in agreement with the preferred alignment [i.e., the interlayer coupling, ferromagnetic (F) or antiferromagnetic (AF)] as in Figs. 17(a) and 17(d), then the effect of the coupling on each of the MnGa films is similar to an applied field in the same direction as the magnetization of that film. It will reduce the internal disorder and thus the resistivity compared to the case where no coupling is present (this would be identical to a free surface). In the opposite case, where the effective alignment frustrates the preferred alignment, Figs. 17(b) and 17(c), the coupling acts as a negative applied field that increases the disorder and contributes to the resistivity. This is schematically indicated by gray shading in Fig. 17.

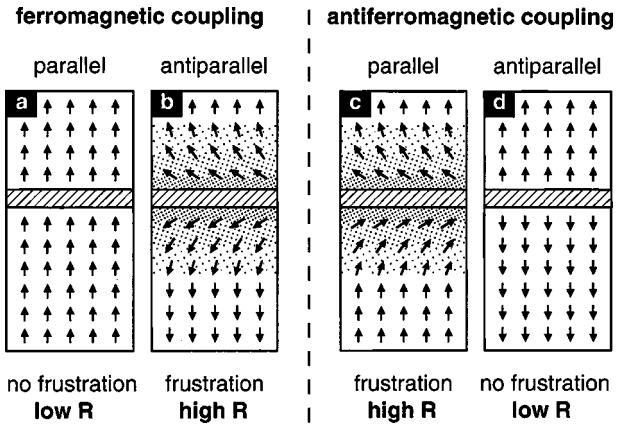

FIG. 17. Schematic representation of the frustration magnetoresistance mechanism. (b), (c) When the momentary alignment (parallel P or antiparallel AP) is opposite to the preferred alignment (ferromagnetic F or antiferromagnetic AF), the induced disorder of the moments near the interface leads to an increase in resistivity. (a), (d) When the momentary alignment is in agreement with the coupling, the coupling field acts as a positive external field that reduces the disorder, lowering the resistivity.

Moreover, since the coupling does not act as a homogenous field, but rather is a interface force, it also creates differences between the top and bottom of each MnGa film. In the cases depicted in Figs. 17(b) or 17(c), the frustrated coupling causes the moments closest to the interface to rotate away from the easy axis, while the moments deeper in the film rotate less. This amounts to a (partial) domain wall between the top and bottom of each MnGa film that runs over the entire area of the sample and contributes to an increase in resistance. An indication of the length scale involved can be found by calculating the domain wall thickness δ. Following Chikazumi,[49] this is given by $\delta=\pi\sqrt{A/K_u}$ for the case of uniaxial anisotropy, with K_u the anisotropy constant and A a coefficient related to the exchange energy. If we consider the Mn sublattice as simple cubic (thus neglecting the tetragonal distortion as well as the influence of Ga on the Mn-Mn exchange), then A is given by $A=\mathcal{J}S^2/a$. Here $S\approx 1$ is the total spin quantum number of each Mn atom, $a\approx 0.30$ nm is the lattice constant (we chose an average value that preserves the volume of the tetragonal cell), and $\mathcal{J}=fk_BT_C$ is the exchange integral with k_B the Boltzmann constant and f a dimensionless prefactor which depends on the crystal structure and the spin quantum number S. No value is given for a simple cubic lattice with $S=1$, and we use the value $f=0.54$ listed for the case $S=\frac{1}{2}$.[49] With $K_u=2.6\times 10^6$ J/m^3 and $T_C=600$ K, this finally results in a domain wall width $\delta_{\mathrm{MnGa}}=7.5$ nm. The small value is mainly a consequence of the large magnetocrystalline anisotropy. Comparing this with the thicknesses of our MnGa trilayers (10 and 8 nm), it is clear that the partial domain wall in the case of frustrated coupling makes up an important part of each MnGa film and can contribute to an increase in resistance.

From Fig. 17 it is obvious that this frustration magnetoresistance mechanism naturally leads to a correlation between not only the sign, but also the amplitude of the interlayer coupling and the magnetoresistance. As the model makes abstraction of the origin of the coupling or the nature of the spacer layer (in fact, it describes resistivity changes *inside* each MnGa film and does not depend on any electrical current passing through the spacer layer), it predicts the same relation for all spacer layers in agreement with Fig. 14(a).

The increase of the negative magnetoresistance due to forced magnetization at room temperature compared to 9 K indicates that the moments are becoming softer, and one would also expect an increase in magnetoresistance due to the frustration mechanism. This is only partly the case in our samples, where Figs. 14(a) and 14(b) show that the slope of $\Delta R/R_{\mathrm{P},0}$ vs J for most samples does not change with temperature.

D. Exchange bias and increased coercivity

Finally, we want to discuss the shape and width of the minor hysteresis loops, since these are crucial for the accuracy of our analysis technique for the interlayer coupling. It is well known that in exchange-biased spin valve structures, where a ferromagnetic film FM is pinned by an antiferromagnetic layer AFM, the exchange bias is often accompanied by an increase in coercive field of the ferromagnet (see Nogues and Schuller[14] for a recent overview). Although the microscopic mechanisms are not completely understood at this moment, the increased coercivity is related to the propagation of domain walls.[50] One possible mechanism (i) is the uniaxial anisotropy induced in the FM film, which increases the energy of the domain walls and reduces their width, thereby making them more sensitive to pinning and increasing the coercive field. Another mechanism (ii) that has been proposed is the reversal of small domains in the antiferromagnet during reversal of the ferromagnet. This leads to irreversible effects that contribute to the coercivity.

The coupling fields and energies in the MnGa trilayers are of the same order as (or even larger than) the typical exchange-bias fields. If the interlayer coupling were to influence the shape or width of the minor hysteresis loops, then the two edges of the minor loops would shift by different amounts, and the center of the loop would no longer be a valid quantitative measure of the interlayer coupling strength. In order to ensure that this is not the case, we have shown the hysteresis loops for extreme values of F and AF coupling strength in Fig. 3. (Here the linear background due to the normal Hall effect is still present; see Fig. 4 for an example after subtraction of the background.) We also have plotted the extracted coercive field H_{c1} of the minor loops for the two trilayers with the strongest coupling in Figs. 6(c) and 11(c). The minor loops are well defined, with 100% remanence, sharp transitions between the P and AP states, and no distortion. The coercive field H_{c1} is constant over the entire wedge, although H_s and H_{c2}^* vary strongly. This shows that the minor loops are not distorted.

The square shape of the hysteresis loops is related to the strong uniaxial magnetocrystalline anisotropy of MnGa ($K_u=2.6\times 10^6$ J/m^3, $\mu_0 H_a=6.4$ T), preventing rotation of the magnetic moments and limiting magnetization reversal to the motion of 180° domain walls, where the coercive field is determined by pinning and/or nucleation events.[34] As the

intrinsic anisotropy and domain wall energy of MnGa films are much larger than any conceivable induced anisotropy by the coupling, the first mechanism (i) that may cause an increase in coercivity in exchange-biased films is negligible in our case. The second possible mechanism—irreversible effects in the antiferromagnet—can also be ruled out since the spacer layer is very thin and only mediates the coupling to the second MnGa film. This is the real biasing layer, as shown by the fact that the bias field changes sign when its magnetization is reversed. Its behavior is automatically monitored during the Hall effect measurements, and the presence of a plateau after the reversal of the soft MnGa film shows that the hard film has not switched yet.

There is, however, one factor that slightly influences the accuracy of our analysis. The small rounding at the leading edge of the transitions indicates that the switching is governed by the pinning and depinning of domain walls, not by the nucleation of new domains which would lead to a transition with a sharp onset and no rounding.[34] For samples with very small AF plateaus [Figs. 3(c) and 3(e)], the leading edges of the AP-to-P transitions are slightly more rounded than those of the P-to-AP transitions. Because we cannot scan the applied field far beyond the AP transition, there are more domain walls left in the AP state that can act as nucleation centers and initiate the switching back to the P state. In order to minimize any bias on our measurement results, we have always scanned the minor loops starting from the AP side and have made the saturation fields for P and AP alignment as symmetric as possible within the constraints of being able to measure all Hall crosses on the section of the wedge under examination. The uniform values of H_{c1} in Figs. 6(c) and 11(c) indicate that this strategy was successful.

VI. CONCLUSIONS

MnGa/Mn_2As/MnGa and MnGa/Mn_2Sb/MnGa trilayers with *magnetic* spacer layers showed an oscillatory dependence of the interlayer exchange coupling strength on the spacer layer thickness, similar to multilayers with metallic, nonmagnetic spacer layers. The *period* of the oscillations is *not related* to the (bulk) long-range magnetic order of the spacer layer material, whereas the *strength* of the coupling *does depend* on the orientation of the easy axis of the spacer layer. The coupling is strong when the easy axis is collinear with the MnGa easy axis and weak when it is orthogonal. These results agree qualitatively with Bruno's quantum interference theory for magnetic interlayer coupling in multilayers with *nonmagnetic* spacer layers and indicate that the bulk long-range order of Mn_2As and Mn_2Sb is modified or quenched in our ultrathin spacer layers. The magnetocrystalline anisotropy, on the other hand, is a result of the local spin-orbit interaction and is not affected by the small layer thickness. The reorientation of the moments in the spacer layer with respect to the MnGa easy axis changes the reflection coefficients at the interfaces and modifies the interlayer coupling strength.

MnGa/GaAs/MnGa trilayers with GaAs spacers without detectable Mn contamination still showed metalliclike behavior, with an oscillatory dependence of the interlayer coupling strength on the spacer layer thickness. This is attributed to the poor crystal structure, where defects and excess As may create additional states in the forbidden gap. We conclude that there is no allowed growth window that combines the low Mn contamination of the GaAs spacer layer with a sufficiently high crystal quality to yield semiconducting properties.

All samples showed a clear correlation between the magnetoresistance and interlayer coupling strength with one universal proportionality ratio for all spacer layer materials. The description by Barnas *et al.* predicts such a correlation for quantum-size effects in the magnetoresistance and interlayer coupling, but it cannot readily explain the universal proportionality ratio we observe. Our frustration magnetoresistance model is a qualitative description that does not depend on the nature of the interlayer coupling or on the choice of spacer layer material. It naturally predicts an identical spacer layer thickness dependence for coupling and magnetoresistance, and a universal proportionality coefficient for all spacer layer materials.

ACKNOWLEDGMENTS

This work, partly supported by the New Energy and Industrial Technology Development Organization (NEDO), was performed in JRCAT under the joint research agreement between NAIR and ATP. W.V.P. acknowledges support during part of this research from the Fund for Scientific Research–Flanders (Belgium).

*Corresponding author. Present address: Imec (MCP-ME), Kapeldreef 75, B-3001 Leuven, Belgium. Electronic address: vanroy@imec.be

†Permanent address: Electrotechnical Laboratory, 1-1-4 Umezono, Tsukuba, Ibaraki 305-8568, Japan.

‡Present address: Sharp Corporation, Advanced Technology Research Laboratories, 2613-1, Ichinomoto, Tenri, Nara 632-8567, Japan.

[1] For an overview, see *Ultrathin Magnetic Structures II*, edited by B. Heinrich and J. A. C. Bland (Springer-Verlag, Berlin, 1994).

[2] B. Briner and M. Landolt, Phys. Rev. Lett. **73**, 340 (1994).

[3] S. S. P. Parkin, Phys. Rev. Lett. **67**, 3598 (1991).

[4] B. Briner, U. Ramsperger, and M. Landolt, Phys. Rev. B **51**, 7303 (1995).

[5] P. Bruno, Phys. Rev. B **49**, 13 231 (1994).

[6] P. Bruno, Phys. Rev. B **52**, 411 (1995).

[7] A. Chaiken, R. P. Michel, and M. A. Wall, Phys. Rev. B **53**, 5518 (1996).

[8] Y. Endo, O. Kitakami, and Y. Shimada, Appl. Phys. Lett. **72**, 495 (1998).

[9] Y. Endo, O. Kitakami, and Y. Shimada, Phys. Rev. B **59**, 4279 (1999).

[10] For a review, see T. Sands, C. J. Palmstrøm, J. P. Harbison, V. G. Keramidas, N. Tabatabaie, T. L. Cheeks, R. Ramesh, and Y. Silverberg, Mater. Sci. Rep. **5**, 99 (1990).

[11] W. Van Roy, H. Akinaga, S. Miyanishi, K. Tanaka, and L. H.

Kuo, Appl. Phys. Lett. **69**, 711 (1996).
[12] W. Van Roy, H. Akinaga, S. Miyanishi, and A. Asamitsu, Appl. Phys. Lett. **71**, 971 (1997).
[13] W. Van Roy, H. Akinaga, and S. Miyanishi, J. Cryst. Growth **201/202**, 698 (1999).
[14] For a review, see J. Nogues and I. K. Schuller, J. Magn. Magn. Mater. **192**, 203 (1999).
[15] J. Barnas and Y. Bruynseraede, Phys. Rev. B **53**, R2956 (1996).
[16] M. Hasegawa and I. Tsuboya, Rev. Electr. Commun. Lab. **16**, 605 (1968). A nonstandard face-centered-tetragonal (fct) unit cell is used, which is rotated by 45° around the *c* axis with respect to the standard body-centered-tetragonal (bct) unit cell.
[17] X.-S. Lu, J.-K. Liang, T.-J. Shi, and M.-G. Zhou, Acta Phys. Sin. **29**, 469 (1980).
[18] A. Sakuma, J. Magn. Magn. Mater. **187**, 105 (1998).
[19] Z. Yang, J. Li, D.-S. Wang, K. Zhang, and X. Xie, J. Magn. Magn. Mater. **182**, 369 (1998).
[20] M. Tanaka, J. P. Harbison, J. De Boeck, T. Sands, B. Philips, T. L. Cheeks, and V. G. Keramidas, Appl. Phys. Lett. **62**, 1565 (1993).
[21] W. Van Roy, H. Akinaga, S. Miyanishi, L. H. Kuo, A. Asamitsu, and K. Tanaka, J. Magn. Soc. Jpn. **21**, 887 (1997).
[22] M. Yuzuri and M. Yamada, J. Phys. Soc. Jpn. **15**, 1845 (1960).
[23] A. E. Austin, E. Adelson, and W. H. Cloud, J. Appl. Phys. **33**, 1356 (1962).
[24] Z. Yang, K. Zhang, and X. Xie, Phys. Rev. B **58**, 339 (1998).
[25] M. K. Wilkinson, N. S. Gingrich, and C. G. Shull, J. Phys. Chem. Solids **2**, 289 (1957).
[26] H. S. Jarrett, P. E. Bierstedt, F. J. Darnell, and M. Sparks, J. Appl. Phys. (Suppl.) **32**, 57S (1961).
[27] F. J. Darnell, W. H. Cloud, and H. S. Jarrett, Phys. Rev. **130**, 647 (1963).
[28] T. Tonegawa, J. Phys. Soc. Jpn. **17**, 1398 (1962).
[29] M. Suzuki, M. Shirai, and K. Motizuki, J. Phys.: Condens. Matter **4**, L33 (1992).
[30] J. H. Wijngaard, C. Haas, and R. A. de Groot, Phys. Rev. B **45**, 5395 (1992).
[31] W. Van Roy, H. Akinaga, and S. Miyanishi, J. Magn. Soc. Jpn. **22**, 605 (1998).
[32] S. Miyanishi, H. Akinaga, W. Van Roy, and K. Tanaka, Appl. Phys. Lett. **70**, 2046 (1997).
[33] L. J. van der Pauw, Philips Res. Rep. **13**, 1 (1958).
[34] W. Van Roy, J. De Boeck, H. Bender, C. Bruynseraede, A. Van Esch, and G. Borghs, J. Appl. Phys. **78**, 398 (1995).
[35] W. Van Roy, H. Akinaga, and S. Miyanishi (unpublished).
[36] H. Fu, L. Ye, K. Zhang, and X. Xie, Surf. Sci. **341**, 273 (1995).
[37] Z. Yang, K. Zhang, and X. Xie, Surf. Sci. **382**, 100 (1997).
[38] Z. Yang, K. Zhang, S. Ke, and X. Xie, Phys. Rev. B **56**, 6727 (1997).
[39] H. Lüth, *Surfaces and Interfaces of Solid Materials*, 3rd ed. (Springer-Verlag, Berlin, 1995), p. 56.
[40] P. Bruno, J. Magn. Magn. Mater. **121**, 248 (1993).
[41] R. A. Hajjar and M. Mansuripur, J. Appl. Phys. **72**, 1528 (1992).
[42] T. R. McGuire and R. I. Potter, IEEE Trans. Magn. **11**, 1018 (1975).
[43] T. Chonan, A. Yamada, and K. Motizuki, J. Phys. Soc. Jpn. **60**, 1638 (1991).
[44] P. E. Bierstedt, F. J. Darnell, W. H. Cloud, R. B. Flippen, and H. S. Jarrett, Phys. Rev. Lett. **8**, 15 (1962).
[45] A. E. Austin, E. Adelson, and W. H. Cloud, Phys. Rev. **131**, 1511 (1963).
[46] An exception would be the case where the net magnetization of the layers changes, e.g., because of an antiferromagnetic-to-ferrimagnetic transition. In this case there is an additional shape anisotropy favoring in-plane moments. For thin films, with a demagnetizing factor $N_d = -1$, the anisotropy field $\mu_0 H_a$ is equal to the net magnetization $\mu_0 M_{\mathrm{sat}}$. In our case this contribution is small compared to the magnetocrystalline anisotropies, e.g., $\mu_0 M_{\mathrm{sat,Mn_2Sb}} = 0.36\,\mathrm{T}$ compared to $\mu_0 H_{a,\mathrm{MnGa}} = 6.4\,\mathrm{T}$.
[47] W. H. Cloud, T. A. Bither, and T. J. Swoboda, J. Appl. Phys. **32**, 55S (1961).
[48] J. Barnas and B. Bulka, Acta Phys. Pol. A **91**, 253 (1997).
[49] S. Chikazumi, *Physics of Magnetism* (Wiley, New York, 1964), Chap. 9, p. 191.
[50] T. C. Schulthess and W. H. Butler, J. Appl. Phys. **85**, 5510 (1999).